

# This is a title

EVAN H. ANDERS,<sup>1</sup> ADAM S. JERMYN,<sup>2</sup> DANIEL LECOANET,<sup>1,3</sup> AND BENJAMIN P. BROWN<sup>4</sup>

<sup>1</sup>*CIERA, Northwestern University, Evanston IL 60201, USA*

<sup>2</sup>*Center for Computational Astrophysics, Flatiron Institute, New York, NY 10010, USA*

<sup>3</sup>*Department of Engineering Sciences and Applied Mathematics, Northwestern University, Evanston IL 60208, USA*

<sup>4</sup>*Department Astrophysical and Planetary Sciences & LASP, University of Colorado, Boulder, CO 80309, USA*

(Received; Revised; Accepted; Published)

Submitted to ApJ

## ABSTRACT

Blah Blah short description

*Keywords:* UAT keywords

## 1. INTRODUCTION

Convection is a crucial heat transport mechanism in essentially all stars (Woosley et al. 2002; Hansen et al. 2004; Christensen-Dalsgaard 2021). Convective dynamics drive many still poorly-understood phenomena in stars. For example, convection drives the magnetic dynamo of the Sun, leading to the host of emergent phenomena known as solar activity (Brun & Browning 2017). Convection is also responsible for compositional mixing, which can modify surface abundances or inject additional fuel into convective cores, thereby extending stellar lifetimes (Salaris & Cassisi 2017). Furthermore, convective motions excite both acoustic and gravity waves, which can be observed and used to constrain the thermodynamic structure of stars (Aerts et al. 2010; Basu 2016). A complete and nuanced understanding of convection is therefore crucial for understanding stellar structure, evolution, and observations.

One aspect of stellar convection which remains poorly understood despite decades of study is the class of mechanisms generally referred to as “convective overshoot.” Broadly, in the stellar structure literature, convective overshoot refers to any mechanism which causes at least compositional mixing beyond the Schwarzschild or Ledoux stable convective boundary. Improved models of overshoot could resolve many discrepancies between observations and structure models. For example, observed surface lithium abundances in the Sun and solar-type stars align poorly with models, which could suggest a need for additional mixing below the solar convection zone (Pinsonneault 1997; Carlos et al. 2019; Dumont et al. 2021). Furthermore, modern spectroscopic observations suggest a lower solar metallicity than previously thought, and models computed with modern metallicity estimates and opacity tables have shallower convection zones than helioseismic observations suggest (Basu & Antia 2004; Bahcall et al. 2005; Vinyoles et al. 2017; Asplund et al. 2021); model and observation discrepancies can be reduced by appropriately incorporating mixing below the convective boundary (Christensen-Dalsgaard et al. 2011). There is also ample evidence from massive stars with core convection that currently-employed prescriptions of convective overshoot are inadequate (Claret & Torres 2018; Jermyn et al. 2018; Viani & Basu 2020; Martinet et al. 2021; Pedersen et al. 2021). Since core convective overshoot increases the reservoir of fuel available for nuclear fusion at each stage in stellar evolution, improved models of core convective boundary mixing could have profound impacts on the post-main sequence evolution and remnant formation of massive stars (Farmer et al. 2019; Higgins & Vink 2020). In order to ensure that models can be evolved on fast (human) timescales, 1D stellar evolution codes rely on simple parameterizations of convective overshoot and mixing beyond convective boundaries (Shaviv & Salpeter 1973; Maeder 1975; Herwig 2000; Paxton et al. 2011, 2013, 2018, 2019).

While some preliminary work has been done to couple 3D dynamical convective simulations with 1D stellar evolution codes (Jørgensen & Weiss 2019), these calculations are currently prohibitively expensive to perform e.g., at every timestep in a stellar evolution calculation. In short, in order to resolve many of the discrepancies between current stellar evolution models and observations, we must come to a more complete, and *parameterizeable* understanding of the manner in which convective motions extend beyond convective boundaries.

The host of mechanisms referred to as “convective overshoot” in the stellar literature fall into two hydrodynamical classes. The first of these classes is, confusingly, also called “convective overshoot” in the fluid dynamics literature and refers to motions which extend beyond the convective boundary and mix chemical compositions but importantly *do not adjust the thermodynamic profile*. The second of these classes is called “convective penetration,” in which convective motions mix the thermodynamic profiles beyond the convective boundary, thereby extending the convective boundary beyond the nominal Schwarzschild or Ledoux one. We will follow a deep history (Zahn 1991; Korre et al. 2019) and use this terminology throughout this work. The primary focus of this work will be on convective penetration, as this mechanism shows promise in aligning observations and models (Christensen-Dalsgaard et al. 2011; Pedersen et al. 2021).

Convective overshoot and penetration have been studied in laboratory experiments and numerical simulations for decades, and has been reviewed by many authors (Marcus et al. 1983; Zahn 1991; Browning et al. 2004; Rogers et al. 2006; Viallet et al. 2015; Korre et al. 2019). Experiments and simulations exhibiting extensive convective penetration in simplified, Boussinesq setups have been studied for decades (Musman 1968; Deardorff et al. 1969; Moore & Weiss 1973), with multiple recent studies suggesting that the penetration depth (or overshoot depth) is highly dependent on the stiffness of the radiative-convective interface (Couston et al. 2017; Toppaladoddi & Wettlaufer 2018; Korre et al. 2019). Some studies in density-stratified or fully compressible, stratified systems (e.g., Hurlburt et al. 1986; Saikia et al. 2000) also found significant penetration depths, with multiple authors finding results suggesting that penetration and overshoot depths were determined by the stiffness of the radiative-convective interface (Hurlburt et al. 1994; Singh et al. 1995; Browning et al. 2004; Dietrich & Wicht 2018). However, a number of studies have contradicted these results, showing little to no dependence on the stiffness (Brummell et al. 2002; Rogers & Glatzmaier 2005). Many modern simulations utilize stellar structure models as inspiration for their experimental setup, and find significant convective overshoot or penetration (Browning et al. 2004; Rogers et al. 2006; Kitiashvili et al. 2016; Brun et al. 2017; Pratt et al. 2017; Higl et al. 2021). Some simulations have found that the extension beyond the convection zone depends strongly on the input flux for their experimental setups (Singh et al. 1998; Käpylä et al. 2007; Tian et al. 2009; Hotta 2017; Käpylä 2019). In this work, we follow the results of these last class of simulations and study how one aspect of the convective flux modifies the extent of the penetration region.

Zahn (1991) theorized that convective penetration should depend only on how steeply the radiative temperature gradient varies at the convective boundary. Following Zahn (1991)’s work, Rempel (2004) derived a semianalytic model and suggested that the boosting of luminosity in stellar experiments compared to reference stars may be leading to wrong estimates of the penetrative dynamics. Indeed, some simulations have shown partial agreement with these ideas. In the limit of low stiffness, the simulations of Hurlburt et al. (1994); Rogers et al. (2006) agree with Zahn’s theory (although at high stiffness they disagree). Some simulations have used the magnitude of the system flux as a control parameter, and indeed found that the penetration depth was dependent on it (Singh et al. 1998; Hotta 2017; Käpylä 2019). These results suggest that Zahn’s theory deserves to be revisited.

In this work, we design two numerical experiments to test the theory of Zahn (1991). We use a modified incompressible, Boussinesq model to study the simplest possible system, and re-derive his theory in our simplified limit. The results of our simulations are in full agreement with Zahn’s theory.

*Specifically, we find that the depth of convective penetration depends on the gradient of the radiative flux near the convective boundary.*

Thus, the penetration depth can be approximated so long as the radiative conductivity, or likewise the opacity, is known at the convective boundary.

We present these findings as follows. In Sec. 2, we describe our modified Boussinesq equations, re-derive the theory of Zahn (1991), and retrieve predictions for our two experimental designs from that theory. In Sec. 3, we describe our simulation setup and parameters. In Sec. 4, we present the results of these simulations, with a particular focus on the depth of the penetrative regions. In Sec. 5, we create and discuss a solar MESA model which uses this theory to

determine the bottom of the solar convection zone. Finally, we discuss how future simulations can put finer constraints on this theory in Sec. 6.

## 2. THEORY

### 2.1. Equations

Throughout this work, we will utilize a modified version of the incompressible Boussinesq equations of motion,

$$\nabla \cdot \mathbf{u} = 0 \quad (1)$$

$$\partial_t \mathbf{u} + \mathbf{u} \cdot \nabla \mathbf{u} = -\frac{1}{\rho_0} \nabla p + \frac{\rho_1}{\rho_0} \mathbf{g} + \nu \nabla^2 \mathbf{u} \quad (2)$$

$$\partial_t T + \mathbf{u} \cdot \nabla T + w \nabla_{\text{ad}} + \nabla \cdot [-k \nabla \bar{T}] = \chi \nabla^2 T' + Q \quad (3)$$

$$\frac{\rho_1}{\rho_0} = -|\alpha|T. \quad (4)$$

Here, the density is decomposed into a (constant) background  $\rho_0$  with fluctuations  $\rho_1$  which appear only in the buoyancy force and depend on the temperature  $T$  and the coefficient of thermal expansion  $\alpha = \partial \ln \rho / \partial T$ . We furthermore define the velocity vector  $\mathbf{u}$ , the viscous diffusivity  $\nu$ , the thermal diffusivity  $\chi$ , the bulk internal heating  $Q$  (as in e.g., Goluskin & van der Poel 2016), and the adiabatic temperature gradient  $\nabla_{\text{ad}}$ . We define  $\nabla_{\text{ad}}$  as a positive value to align with stellar structure conventions; thus marginal stability is achieved when  $\partial_z T = -\nabla_{\text{ad}}$ . These equations are similar to those derived by Spiegel & Veronis (1960) and utilized by e.g., Korre et al. (2019), but we allow the mean temperature profile  $\bar{T}$  to carry a radiative flux  $F_{\text{rad}} = -k \nabla \bar{T}$ , where  $k$  is a radiative diffusivity which can vary with height. The classic Boussinesq thermal diffusion term  $\chi \nabla^2 T'$  therefore carries no flux and acts only on the fluctuations away from the mean temperature profile,  $T' \equiv T - \bar{T}$ ; throughout this work, we will represent horizontal averages with bars ( $\bar{\phantom{x}}$ ) and primes ( $'$ ) represent fluctuations away from those horizontal means. Throughout this work, we will consider Cartesian coordinates  $(x, y, z)$ , but this analysis is generalizable to spherical geometry. We will furthermore assume a model in which an unstable convection zone sits below a stable radiative zone, but this analysis also holds for the inverted problem.

### 2.2. Vertical momentum equation balances

Assuming a vertical and uniform gravitational acceleration  $\mathbf{g} = -g\hat{z}$ , the vertical component of Eqn. 2 with Eqn. 4 is

$$\partial_t w + (\mathbf{u} \cdot \nabla) w = -\frac{1}{\rho_0} \partial_z p + |\alpha|gT + \nu \nabla^2 \mathbf{u}. \quad (5)$$

We next horizontally average this equation; under the assumption that  $\bar{w} = 0$  at some height (e.g., at an impenetrable boundary), Eqn. 1 requires  $\bar{w} = 0$  everywhere. The horizontally-averaged equation is therefore

$$\frac{1}{\rho_0} \frac{d\bar{p}}{dz} = |\alpha|g\bar{T} - \overline{(\mathbf{u} \cdot \nabla)w} + \nu \overline{\nabla_h^2 \mathbf{u}}, \quad (6)$$

where  $\nabla_h^2 = \partial_x^2 + \partial_y^2$ . At this point we decompose  $\bar{p} = \bar{p}_s + \bar{p}_d$ , where  $p_s$  is the “structure” component of the pressure whose gradient balances the buoyant gradient (providing hydrostatic balance), and  $p_d$  is the dynamical pressure whose mean balances the mean contributions of advection and dissipation. Accordingly, we define  $\tilde{p} \equiv p - \bar{p}_s$ , removing the mean structure component of the pressure. This construction leaves fluctuations ( $p'$  and  $\bar{p}_d$ ) which are set by the convective dynamics. Taking a time-average of Eqn. 5 and assuming that convection reaches a statistically stationary state and that viscous dissipation is unimportant (which is a common assumption, but may not always apply in stellar contexts per Currie & Browning 2017), we retrieve

$$\frac{1}{\rho_0} \frac{\partial \tilde{p}}{\partial z} = |\alpha|gT' - (\mathbf{u} \cdot \nabla)w. \quad (7)$$

In other words, convection reaches a state in which fluctuating buoyancy forces and nonlinear advection come into a balance and saturate at similar magnitudes. The pressure gradient rises to a similar magnitude to regulate the flows and ensure Eqn. 1 is satisfied (and a similar argument could be made for e.g., anelastic convection). As a result, we can estimate that each of the terms in this equation have similar magnitudes,

$$\frac{1}{\rho_0} \frac{\partial \tilde{p}}{\partial z} \sim |\alpha|gT' \sim (\mathbf{u} \cdot \nabla)w. \quad (8)$$

### 2.3. Kinetic energy & the velocity-flux link

Taking an inner product of the velocity and Eqn. 2 (after removing  $\bar{T}$  and  $\bar{p}_s$ , as in Eqn. 7) reveals the kinetic energy equation,

$$\frac{\partial}{\partial t} \left( \frac{u^2}{2} \right) + \nabla \cdot \left[ \mathbf{u} \left( \frac{u^2}{2} + \frac{\tilde{p}}{\rho_0} \right) - \nu \mathbf{u} \times \boldsymbol{\omega} \right] = \alpha g w T' - \nu \omega^2, \quad (9)$$

where  $\boldsymbol{\omega} = \nabla \times \mathbf{u}$  is the vorticity and  $u^2 = \mathbf{u} \cdot \mathbf{u}$  &  $\omega^2 = \boldsymbol{\omega} \cdot \boldsymbol{\omega}$ . Again neglecting viscosity, averaging horizontally and in time, and assuming a statistically stationary state, we retrieve

$$\frac{d}{dz} \left[ \frac{\overline{wu^2}}{2} + \frac{\overline{w\tilde{p}}}{\rho_0} \right] = \alpha g \overline{F_{\text{conv}}}, \quad (10)$$

where  $\overline{F_{\text{conv}}} = \overline{wT'}$ . At this point we now assume that the velocities are vertically dominated or isotropic so that  $u^2 \sim w^2$ . We furthermore assume that the balance in Eqn. 8 is roughly correct, so that  $\overline{w\tilde{p}} \sim \rho_0 \overline{w^3}$ . Under these assumptions, we retrieve

$$\frac{d\overline{w^3}}{dz} \sim \alpha g \overline{F_{\text{conv}}} \Rightarrow \frac{d\overline{w^3}}{dz} \approx \varsigma \alpha g \overline{F_{\text{conv}}}, \quad (11)$$

where  $\varsigma$  is a fudge factor which describes the quality of the assumptions we have made, and the fact that e.g.,  $w^2 < u^2$ , the balance of Eqn. 8 likely only holds to a factor of a few, etc.. This equation is logically analogous to one used between Eqn. 3.8 & 3.9 of Zahn (1991), but we have not relied upon the assumption of a vertically invariant convective planform which likely does not hold for turbulent dynamics. Eqn. 11 is also intuitively satisfying; it says that roughly  $\overline{w^3} \sim \overline{F_{\text{conv}}}$ , which fits intuition from mixing length theory.

### 2.4. A flux-based penetration argument

According to an equation similar to Eqn. 11, Zahn (1991) theorized that the size of the convection zone is determined by the horizontally-averaged energy fluxes. Assuming convection reaches a time-stationary state, we horizontally-average and vertically integrate Eqn. 3 to find

$$\overline{F_{\text{tot}}} = \overline{F_{\text{rad}}} + \overline{F_{\text{conv}}} = \int Q dz + F_{\text{bot}}, \quad (12)$$

where  $F_{\text{bot}}$  is the flux carried at the bottom of the considered domain, and  $\overline{F_{\text{tot}}}$  is the total flux, which can vary in height due to the heating  $Q$ . We next assume that convection penetrates above the Schwarzschild boundary of the convection zone at  $z = L_s$  and mixes the temperature gradient to the adiabatic in the region  $z \in [L_s, L_s + \delta_p]$ , where  $\delta_p$  is the penetration depth. This assumption specifies the convective flux in the penetrative region,

$$\overline{F_{\text{conv}}}(z \in [L_s, L_s + \delta_p]) = F_{\text{tot}} - \overline{F_{\text{rad,ad}}} = F_{\text{tot}} - k \nabla_{\text{ad}}. \quad (13)$$

At this point it is useful to define the radiative gradient,  $\nabla_{\text{rad}} = F_{\text{tot}}/k$ . Within the penetrative region,  $\nabla_{\text{ad}} > \nabla_{\text{rad}}$ , so Eqn. 13 requires  $\overline{F_{\text{conv}}} < 0$ .

With the convective fluxes defined, Eqn. 11 can be integrated over the depth of the convection zone (from  $W = 0$  at  $z = 0$  to  $W = W_0$  at  $z = L_s$ ), as well as over the penetration zone (from  $W = W_0$  at  $z = L_s$  to  $W = 0$  at  $z = L_s + \delta_p$ ). We assume however that the convective dynamics are not identical in the convection zone (CZ) and penetration zone (PZ), so that the fudge factor  $\varsigma$  differs between the two zones. Taking the ratio of these two integrals, we find

$$\mathcal{D} \equiv \frac{\varsigma_{\text{CZ}}}{\varsigma_{\text{PZ}}}, \quad \frac{\int_{\text{PZ}} \overline{F_{\text{conv}}} dz}{\int_{\text{CZ}} \overline{F_{\text{conv}}} dz} \approx -\mathcal{D}. \quad (14)$$

This equation represents the central result of Zahn (1991)'s theory: the ratio of the vertically integrated convective fluxes in the PZ and CZ is directly linked to some constant which reflects the difference in the dynamics between the CZ and the PZ ( $\mathcal{D}$ ). More importantly, this integral ratio sets the size of the PZ.

Eqn. 14 is unfortunately not intuitively satisfying. In order to derive a specific prediction for the PZ depth, it is necessary to specify the vertical shape of  $\overline{F_{\text{conv}}}$ . We will study two cases in this work, laid out below. In both of these cases, we will define a nondimensional ‘‘Penetration Parameter,’’

$$\mathcal{P} \equiv -\frac{\overline{F_{\text{conv}}}(z = L_s - \epsilon)}{\overline{F_{\text{conv}}}(z = L_s + \epsilon)}, \quad (15)$$

which is the negative ratio of the convective flux some equidistant length  $\epsilon$  both above and below the Schwarzschild convective boundary  $L_s$  (assuming the region above the boundary is an adiabatic penetrative zone).

#### 2.4.1. Case I: Discontinuous flux

We first consider a model which satisfies

$$\overline{F_{\text{conv}}}(z) = F_{\text{cz}} \begin{cases} 1 & z \leq L_{\text{cz}}, \\ -\mathcal{P}_D^{-1} & z > L_{\text{cz}} \end{cases}. \quad (16)$$

Here,  $F_{\text{cz}}$  is a (constant) value of flux carried in the convection zone and  $\mathcal{P}_D$  is the penetration parameter (subscript D for discontinuous case). Plugging this functional form of the flux into Eqn. 14, and integrating the convection zone from  $z = 0$  to  $z = L_s$  and the penetration zone from  $z = L_s$  to  $z = L_s + \delta_p$ ,

$$\frac{\delta_p}{L_s} = \mathcal{P}_D \mathcal{D}. \quad (17)$$

We see that the size of the penetration region is linearly proportional to  $\mathcal{P}_D$  and is a function of the structure of the convective dynamics ( $\mathcal{D}$ ). Intuitively, this result makes sense: as  $\mathcal{P}_D$  grows, the magnitude of  $\overline{F_{\text{conv}}}$  and the breaking force of buoyancy in the PZ shrink, resulting in larger penetrative regions.

#### 2.4.2. Case II: Piecewise linear flux

We next assume that  $\overline{F_{\text{conv}}}(z)$  is not discontinuous at the CZ-PZ boundary, but that its derivative may be,

$$\overline{F_{\text{conv}}}(z) = \frac{\partial F_{\text{rad}}}{\partial z} \Big|_{\text{cz}} \begin{cases} (L_p - z) & z \leq L_p, \\ -\mathcal{P}_L^{-1}(z - L_p) & z > L_p \end{cases}, \quad (18)$$

where  $(\partial F_{\text{rad}}/\partial z)|_{\text{cz}}$  is a constant and  $\mathcal{P}_L$  is the penetration parameter (subscript L for linear case). Again, solving Eqn. 14 with this functional form of the flux, we retrieve

$$\frac{\delta_p}{L_p} = \sqrt{\mathcal{P}_L \mathcal{D}}, \quad (19)$$

which aligns with the prediction of Zahn (1991)'s Eqn. 3.13 when we take  $\mathcal{P}_L = 1$ .

In this work, we will test the predictions of Eqns. 17 and 19. Our goals are to see if the predicted scalings with the penetration parameter  $\mathcal{P}$  are realized in simulations, and to measure preliminary values for  $\mathcal{D}$  in local simulations.

### 3. SIMULATION DETAILS

We nondimensionalize Eqns. 1-4 on the length scale of the Schwarzschild-defined convection zone ( $L_s$ ), the timescale of freefall across that convection zone ( $\tau_{\text{ff}}$ ), and the temperature scale of the internal heating over that freefall time ( $\Delta T$ ),

$$\begin{aligned} T^* &= (\Delta T)T = Q_0 \tau_{\text{ff}} T, & \partial_{t^*} &= \tau_{\text{ff}}^{-1} \partial_t = \left( \frac{\alpha g Q_0}{L_s} \right)^{1/3} \partial_t, & \nabla^* &= L_s^{-1} \nabla, & \mathbf{u}^* &= u_{\text{ff}} \mathbf{u} = (\alpha g Q_0 L_s^2)^{1/3} \mathbf{u}, \\ p^* &= \rho_0 u_{\text{ff}}^2 \varpi, & k^* &= (L_s^2 \tau_{\text{ff}}^{-1}) k, & Q^* &= Q_0 Q, & \mathcal{R} &= \frac{u_{\text{ff}} L_s}{\nu}, & \text{Pr} &= \frac{\nu}{\chi}. \end{aligned} \quad (20)$$

For convenience, here we define quantities with  $*$  (e.g.,  $T^*$ ) as being the “dimensionful” quantities of Eqns. 1-4. Going forward, quantities without  $*$  (e.g.,  $T$ ) will be dimensionless. The dimensionless equations of motion are therefore

$$\nabla \cdot \mathbf{u} = 0 \quad (21)$$

$$\partial_t \mathbf{u} + \mathbf{u} \cdot \nabla \mathbf{u} = -\nabla \varpi + T \hat{z} + \mathcal{R}^{-1} \nabla^2 \mathbf{u} \quad (22)$$

$$\partial_t T + \mathbf{u} \cdot \nabla T + w \nabla_{\text{ad}} + \nabla \cdot [-k \nabla T] = (\text{Pr} \mathcal{R})^{-1} \nabla^2 T' + Q. \quad (23)$$

We construct a domain in the range  $z \in [0, L_z]$  where in this work we choose  $L_z \geq 2$  so that the domain contains at least two convection zone length scales according to the Schwarzschild criterion. We decompose the temperature field into a background and fluctuations,  $T(x, y, z, t) = T_0(z) + T_1(x, y, z, t)$ . For boundary conditions, we impose impenetrable, no-slip boundary conditions at the top and bottom of the box so that  $\mathbf{u} = 0$  at  $z = [0, L_z]$ . We also impose a fixed-flux boundary at the bottom of the box ( $\partial_z T_1 = 0$  at  $z = 0$ ) and a fixed temperature boundary at the top of the domain ( $T_1 = 0$  at  $z = L_z$ ).

We impose a constant internal heating which spans only part of the convection zone,

$$Q = \begin{cases} 0 & z < 0.1 \text{ or } z \geq 0.1 + \delta_H, \\ |Q_{\text{mag}}| & 0.1 \leq z \leq 0.1 + \delta_H \end{cases}. \quad (24)$$

The integrated value of the flux through the system from the heating is therefore  $F_H(z > 0.1 + \delta_H) = \int_0^z Q_{\text{mag}} dz = Q_{\text{mag}} \delta_H$ . Throughout this work we choose  $Q_{\text{mag}} = 1$  and  $\delta_H = 0.2$  so  $F_H = 0.2$ . We offset this heating from the bottom boundary to  $z = 0.1$  to avoid heating within the bottom impenetrable boundary layer where velocities go to zero and  $k$  is small; this prevents strong temperature gradients from establishing there. We assume that the (adiabatic) temperature gradient at the bottom boundary carries some flux,  $F_{\text{bot}} = \zeta F_H$  and we choose  $\zeta = 10^{-3}$  so that most of the flux in the convection zone is carried by the convection.

In our equations, we expect the volume-average convective velocities to depend on the magnitude of the heating,  $\langle \mathbf{u} \rangle \approx Q_{\text{mag}}^{1/2} \approx 1$ , so the characteristic convective frequency  $f_{\text{conv}} \approx \langle \mathbf{u} \rangle L_{\text{cz}} \approx 1$ . We want to allow the stiffness of the radiative-convective interface to be a control parameter. The stiffness is defined,

$$\mathcal{S} \equiv \frac{N^2}{f_{\text{conv}}} \approx N^2, \quad (25)$$

where  $N^2$  is the Brunt-Väisälä frequency in the radiative zone. In our nondimensionalization,  $N^2 = \nabla_{\text{ad}} - \nabla_{\text{rad}}$  where  $\nabla_{\text{rad}} = F_{\text{tot}}/k$ , so by choosing a value of the stiffness we set the magnitude of the background temperature gradient,  $\partial_z T_0$  which in turn sets the value of  $k$  in the radiative zone.

The crucial place in which our model differs from that of prior work is that we define a “penetration parameter,”  $\mathcal{P}$ , according to Eqn. 15. We construct our experiments so that  $\mathcal{P}$  and  $\mathcal{S}$  can be varied separately. We suspect that many past experiments have implicitly set  $\mathcal{P} \approx \mathcal{S}^{-1}$ .

Aside from  $\mathcal{S}$  and  $\mathcal{P}$ , the two remaining control parameters that control our experiments determine the degree of turbulence. The value of  $\mathcal{R}$  roughly corresponds to the value of the peak Reynolds number  $\text{Re} = \mathcal{R}|\mathbf{u}|$  measured in the simulations, and we set the ratio of the diffusivities  $\text{Pr} = 0.5$  throughout this work. Astrophysical convection is in the limit of  $\text{Pr} \ll 1$  (Garaud 2021); we choose a modest value of  $\text{Pr}$  which slightly separates the scales between thermal and viscous structures while still allowing us to achieve convection with large Reynolds and Péclet numbers.

### 3.1. Case I: Discontinuous flux

Most of the simulations in this paper study simulations with a discontinuous convective flux at the Schwarzschild convective boundary. We achieve this by constructing a discontinuous radiative conductivity,

$$k_D(z) = \begin{cases} k_{\text{CZ}} & z < 1 \\ k_{\text{RZ}} & z \geq 1 \end{cases}. \quad (26)$$

Leaving  $\mathcal{S}$  and  $\mathcal{P}_D$  as free parameters and requiring that the adiabatic gradient can carry the  $F_{\text{bot}}$  at  $z = 0$  and that the radiative gradient can carry the flux for  $z \geq 1$  specifies this system fully,

$$k_{\text{RZ}} = \frac{\delta_H}{\mathcal{S}\mathcal{P}_D}, \quad k_{\text{CZ}} = k_{\text{RZ}} \frac{1}{1 + \zeta + \mathcal{P}_D^{-1}}, \quad \nabla_{\text{ad}} = Q_{\text{mag}} \mathcal{S} \mathcal{P}_D (1 + \zeta + \mathcal{P}_D^{-1}), \quad \nabla_{\text{rad}} = \nabla_{\text{ad}} - Q_{\text{mag}} \mathcal{S}. \quad (27)$$

We study three sweeps through the  $(\mathcal{P}_D, \mathcal{S}, \mathcal{R})$  parameter space in this paper (one in which we vary each parameter while holding the other parameters constant). We use “Reference values” of  $\mathcal{P}_D = 4$ ,  $\mathcal{S} = 10^3$ , and  $\mathcal{R} = 400$ ; all of our parameter space sweeps pass through this point in the three-dimensional parameter space. As in section 2.4.1, we expect  $\delta_p \propto \mathcal{P}_D$ .



### 3.2. Case II: Piecewise linear flux

We additionally study a select few simulations where the flux’s gradient may be discontinuous at the Schwarzschild convective boundary. We achieve this by constructing a radiative conductivity with a piecewise discontinuous gradient,

$$\partial_z k = \partial_z k_0 \begin{cases} 1 & z < 1 \\ \mathcal{P}_L^{-1} & z \geq 1 \end{cases} \quad (28)$$

Since  $k$  varies with height, the value of  $\mathcal{S}$  and  $\mathcal{P}$  also vary with height; we specify their values at  $z = 2$ . by this choice, we require

$$\partial_z k_0 = \frac{\delta_H}{L_{cz}\mathcal{S}\xi}, \quad k_b = \frac{\delta_H\zeta}{\mathcal{S}\xi}, \quad \nabla_{\text{ad}} = Q\mathcal{S}\xi, \quad (29)$$

where  $\xi \equiv 1 + \mathcal{P}_L(1 + \zeta)$ . In these simulations, we hold  $\mathcal{S} = 10^3$  and  $\mathcal{R} = 800$  while varying  $\mathcal{P}_L$ . As in section 2.4.2, we expect  $\delta_p \propto \mathcal{P}_L^{1/2}$ .

### 3.3. Numerics

We time-evolve equations 21-23 using the Dedalus pseudospectral solver (Burns et al. 2020)<sup>1</sup> using timestepper RK443 (Ascher et al. 1997). All fields are represented as spectral expansions of  $n_z$  Chebyshev coefficients in the vertical ( $z$ ) direction and as  $(n_x, n_y)$  Fourier coefficients in the horizontal ( $x, y$ ) directions; our domains are therefore horizontally periodic. The aspect ratio of our domains is two so that  $x \in [0, L_x]$  and  $y \in [0, L_y]$  with  $L_x = L_y = 2L_z$ . To start our simulations, we add random noise temperature perturbations with a magnitude of  $10^{-3}$  to a background temperature profile  $\bar{T}$ ; we discuss the choice of  $\bar{T}$  in appendix A. We produce the figures in this paper using matplotlib (Hunter 2007; Caswell et al. 2021). All of the Python scripts used to run the simulations in this paper and to create the figures in this paper are publicly available in a git repo, found at [CITE].

Spectral methods with finite coefficient expansions cannot capture true discontinuities. In order to approximate discontinuous functions such as Eqns. 24, 26, 28, we must use smooth transitions. To create these smooth transitions, we define an approximate Heaviside step function using the error function,

$$H(z; z_0, \delta_w) = \frac{1}{2} \left( 1 + \operatorname{erf} \left[ \frac{z - z_0}{\delta_w} \right] \right). \quad (30)$$

In the limit of that  $\delta_w \rightarrow 0$ , this function behaves identically to the classical Heaviside function centered at  $z_0$ . While constructing Eqn. 24 and Eqn. 28, we use  $\delta_w = 0.02$ ; while constructing Eqn. 26 we use  $\delta_w = 0.075$ . In all other cases, we use  $\delta_w = 0.05$ .

### 3.4. Penetration depth measurements

In our evolved simulations, we find that the penetrative region has a nearly adiabatic stratification  $\nabla \approx \nabla_{\text{ad}}$ . In order to characterize the vertical extent of the penetrative (and subsequent overshoot) region, we measure how drastically  $\nabla$  has departed from  $\nabla_{\text{ad}}$ . We define the difference between the adiabatic and radiative gradient,

$$\Delta\nabla \equiv \nabla_{\text{ad}}(z) - \nabla_{\text{rad}}(z). \quad (31)$$

We measure penetration and overshoot depths in terms of “departure points,” that is, points at which the realized temperature gradient  $\nabla$  has evolved away from the adiabatic  $\nabla_{\text{ad}}$  by some fraction  $f < 1$ . Specifically,

$$1 + \delta_f = \max(z) \mid \nabla > \nabla_{\text{ad}} - f\Delta\nabla. \quad (32)$$

In this work, we measure the 10% ( $\delta_{0.1}$ ), 50% ( $\delta_{0.5}$ ), and 90% ( $\delta_{0.9}$ ) departure points, which are respectively at the top of the penetration zone, in the middle of the overshoot zone, and at the top of the overshoot zone. We find that these measurements based on the (slowly-evolving) thermodynamic profile are more robust and straightforward than many previous dynamically-based prescriptions (see e.g., Pratt et al. 2017, for a nice discussion).

<sup>1</sup> we use X version

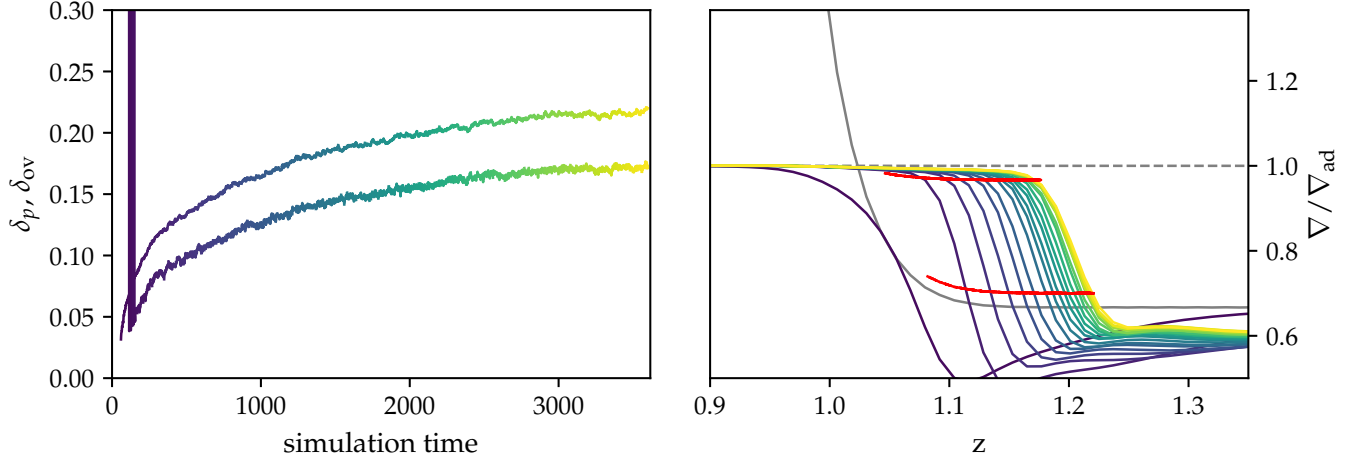


**Figure 1.** (Top panel) we show traces of the time evolution of the points in the simulation where  $\nabla$  has departed from  $\nabla_{ad}$  by 10% (bottom curve) and 90% (top curve) of  $\Delta = \nabla_{ad} - \nabla_{rad}$ . Time is plotted on the x-axis in freefall units which are roughly equal to convective overturn times; the color of the line represents the simulation time. While this evolution is initially fast (changing noticeably over hundreds of overturn times), as the convection zone approaches its final size its evolution drastically slows down. (Bottom panel) The vertical profile of  $\nabla/\nabla_{ad}$  is plotted against height at different times (where the color denotes the time and matches the color of the top panel). The (constant) value of  $\nabla_{ad}$  is denoted by the horizontal dashed grey line, and the value of  $\nabla_{rad}$  is denoted by the solid grey line. The 10% and 90% departure curves from the top panel are overplotted as red lines.

## 4. RESULTS

### 4.1. Qualitative description of simulation evolution

In Fig. 1, we show the time evolution of a Case I simulation with  $\mathcal{R} = 400$ ,  $\mathcal{S} = 10^3$ , and  $\mathcal{P}_D = 2$  (TODO: change to 4) whose initial conditions set  $\nabla = -\partial_z T$  equal to  $\nabla_{ad}$  in the convection zone ( $z < 1$ ) and equal to  $\nabla_{rad}$  in the radiative zone ( $z > 1$ ). Initially, over hundreds of overturn times, the front of the convection zone drastically advances past the Schwarzschild boundary of the convection zone at  $z = 1$ . As the convection zone advances and mixes  $\nabla \rightarrow \nabla_{ad}$  within itself; this steepening of  $\nabla$  within the PZ is accompanied by a flattening of  $\nabla < \nabla_{rad}$  at the base of the RZ along the front of the CZ. This flattening of  $\nabla$  increases the value of  $N^2 = \nabla_{ad} - \nabla$  at the front of the convection zone, slowing the advancement of the convection zone until this disequilibrium state diffuses to the top boundary of the simulation. This stiffer radiative-convective interface, combined with the presence of an increasingly growing breaking region in the form of the PZ slows the advancement of the convective front and the final equilibration of the top boundary of the convection zone takes thousands of convective overturn times.

In Fig. 2, we display instantaneous vertical slices through a turbulent simulation with  $\mathcal{P}_D = 4$  and  $\mathcal{S} = 10^3$  in an equilibrated state. We see that strong convective dynamics (viewed in the left vertical velocity panel) extend beyond the Schwarzschild boundary of the convection zone into a penetration zone. However, there is still a stable radiative zone with small vertical velocity perturbations into which the convection does not extend. On the right, we see that hot upwellings in the convective dynamics are turned into cold upwellings in the PZ as a result of effective cooling from the sharp change in  $k$  around the Schwarzschild boundary of the convection zone. These upwellings impinge upon the stable radiative zone and excite gravity waves [cf., CITE], but our focus in this work is on the nature of the PZ where convective velocities and temperature anomalies are oppositely signed.

### 4.2. Measured penetration zone scalings

In Fig. 3, we plot measured values of the penetration depth from Case I (discontinuous  $k$ ) simulations, quantified by the 10%, 50%, and 90% departure points from  $\nabla_{ad}$ . In the left panel we plot the predicted scaling with  $\mathcal{P}_D$  from Eqn. 17 as well as the measured penetration depths from our simulations. We find good agreement with the theory, and at large values of  $\mathcal{P}_D$  find equilibrated states in which the PZ is equal to or greater in size than the nominal convection zone (of unit depth). We find that the value of  $\mathcal{P}_D$  is the primary parameter whose value modifies the



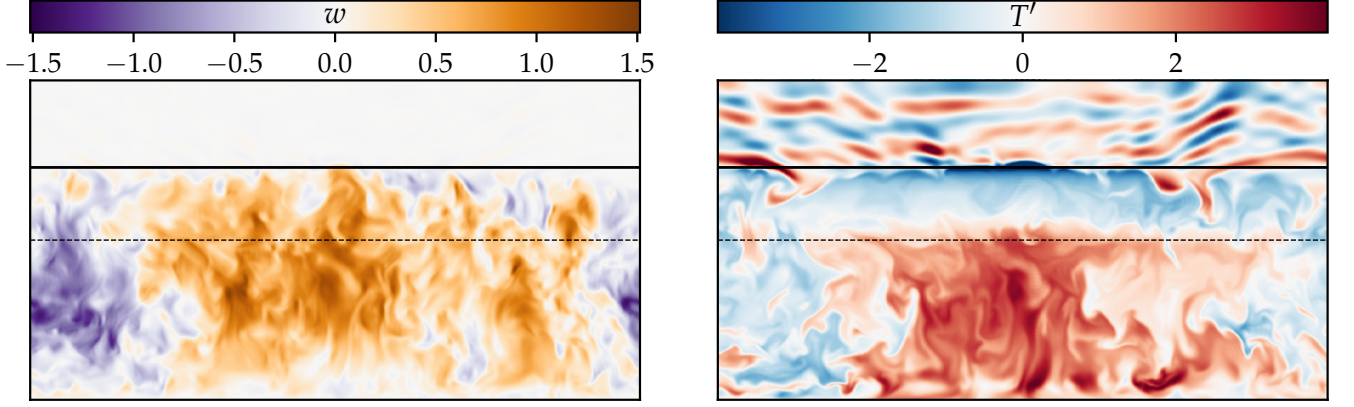


**Figure 2.** Instantaneous snapshots of a vertical slice through the simulation with  $\mathcal{R} = 3.2 \times 10^3$ ,  $\mathcal{P}_D = 4$  and  $\mathcal{S} = 10^3$  are shown. In both panels, the nominal Schwarzschild top of the convection zone where  $\nabla_{\text{ad}} = \nabla_{\text{rad}}$  is displayed as a dashed horizontal line, and the top of the convection zone where  $\nabla$  departs from  $\nabla_{\text{ad}}$  by 10% of  $\Delta = \nabla_{\text{ad}} - \nabla_{\text{rad}}$  is shown as a solid horizontal line. (Left) The vertical velocity is shown; convective upflows extend far past the Schwarzschild boundary of the convection zone but stop abruptly where  $\nabla$  departs from  $\nabla_{\text{ad}}$ . (Right) Temperature perturbations away from  $\bar{T}$  are shown; these perturbations are normalized by their standard deviation at each height in order to make both the convective features (below the solid black line) and internal gravity waves excited by the convection (above) visible. Unlike in the vertical velocity slice, we see that the temperature perturbations switch sign at the Schwarzschild boundary of the convection zone (the dashed horizontal line); buoyancy thus switches from an accelerating force to a braking force.

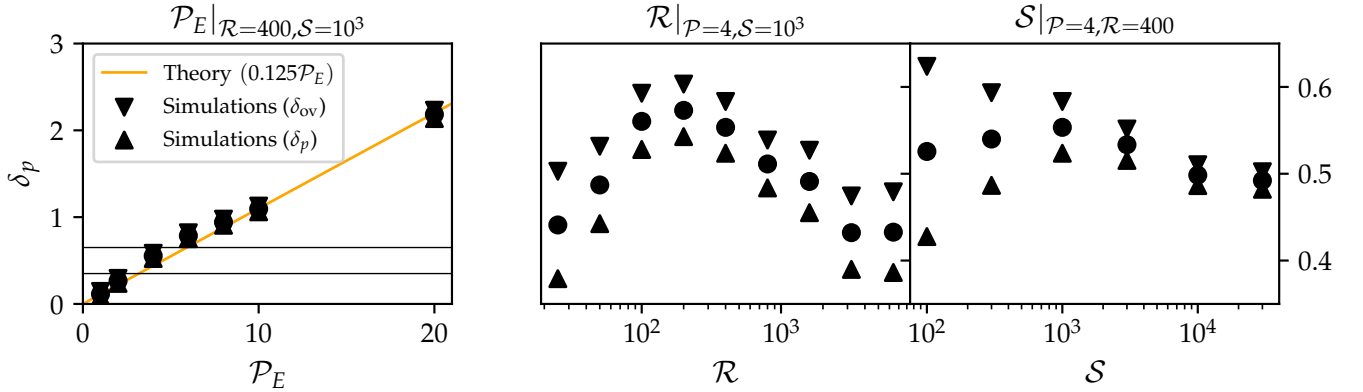


**Figure 3.** We plot penetration depths against  $\mathcal{P}_D$  (left, at constant  $\mathcal{R}$ ,  $\mathcal{S}$ ),  $\mathcal{R}$  (center, at constant  $\mathcal{P}_D$ ,  $\mathcal{S}$ ), and  $\mathcal{S}$  (right, at constant  $\mathcal{P}_D$ ,  $\mathcal{R}$ ). Up-triangles are the location of 10% departure, down-triangles are the location of 90% departure, and circles are the location of 50% departure. In the left panel, we plot a line corresponding to the theory of Eqn. 17. We find that the penetration depth is a strong, roughly linear function of  $\mathcal{P}_E$ , in good agreement with the theory. The horizontal lines in the left panel represent the full range of the right two panels; the effects of varying  $\mathcal{S}$  and  $\mathcal{R}$  are secondary to the effects of  $\mathcal{P}$ . In the center panel, we see that the penetration depth increases at low  $\mathcal{R}$  as laminar dynamics give way to time-evolving dynamics. As we increase the turbulence, the penetration depth decreases weakly and appears to asymptote in the turbulent regime. In the right panel, we see little change in the 50% departure point, and we see that 10% and 90% departure points converge to the central point as a function of stiffness.

height of the convection zone. While not presented in this work, we performed limited 2D simulations and found similar scalings, but with larger penetration zones for the same parameters in 2D than in 3D.

In the center and rightmost panels of Fig. 3, we focus on modifications to the measured penetration depths achieved by varying  $\mathcal{R}$  (turbulence) and  $\mathcal{S}$  (stiffness). We find that the penetration depth is smaller at very low (laminar) values of  $\mathcal{R}$  and at high (turbulent) values of  $\mathcal{R}$ , with a peak at moderate values (for which dynamics are interesting and non-stationary, but not as turbulent as e.g., Fig. 2). Our data suggest that the penetration depth asymptotes as  $\mathcal{R}$

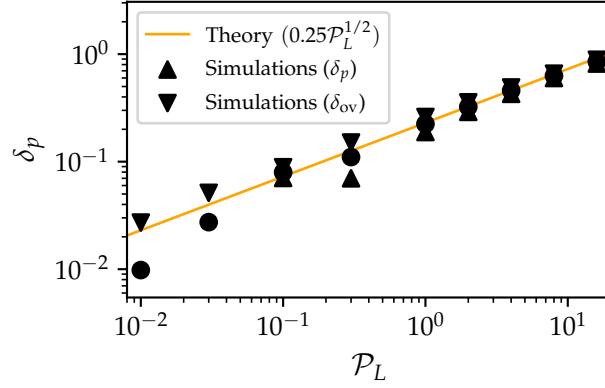


**Figure 4.** Similar to Fig. 3, but for the Case II “linear” simulations where the slope of  $k$  is discontinuous at the Schwarzschild point. We plot a line corresponding to the theory of Eqn. 19 as well as the 10% (up triangle), 50% (circle), and 90% (down triangle) departure points. We find that the theory describes our simulation measurements well. We note that at small values of  $\mathcal{P}_L \lesssim 10^{-1}$ , the 10% departure point approaches the Schwarzschild boundary of the convection zone, approaching zero and not appearing on this plot.

increases and so our results should be relevant for the astrophysical case in which  $\mathcal{R} \rightarrow \infty$ . We note however that these simulations are expensive to run and cannot be converged to the same degree of confidence as the simulations for which  $\mathcal{R} \lesssim 10^3$ , which we run for thousands of overturn times. We find that mean penetration depth (the 50% departure point) shows little dependence on the stiffness (circles in the right panel). However, the depth of the transition region from the PZ to the RZ shows a strong dependence on stiffness. In stars, the stiffness is roughly determined by the Mach number ( $\text{Ma}^{-2} \sim \mathcal{S}$ ), so for low-Mach convective stellar flows, the boundary of the PZ and RZ can likely be reasonably approximated as a step function in  $\nabla$ .

Finally, in Fig. 4, we plot penetration depths as a function of  $\mathcal{P}_L$  for the “linear” Case II simulations. We compare these depths to the theory of Eqn. 19. We hold  $\mathcal{R} = 800$  and  $\mathcal{S} = 10^3$  constant for these simulations. As in the discontinuous simulations, we find excellent agreement between the simulations and the theory.

Our simulation results present a strong case for the validity of Zahn (1991)’s theory. The generalized Eqn. 14, and its solution for our simulation setups in Eqns. 17 & 19, describe our data well. In addition to the flux-based penetration parameter  $\mathcal{P}$ , the theory of Eqn. 14 depends on the horizontal structure of the flux-carrying convective flows. In this work, from the theory lines plotted in Figs. 3 & 4, we find

$$\frac{(\bar{h}^3/\bar{h}^2)_{\text{PZ}}}{(\bar{h}^3/\bar{h}^2)_{\text{CZ}}} \approx 0.125 \text{ (Case I: Discontinuous)}, \quad \frac{(\bar{h}^3/\bar{h}^2)_{\text{PZ}}}{(\bar{h}^3/\bar{h}^2)_{\text{CZ}}} \approx 0.0625 \text{ (Case II: Linear)}. \quad (33)$$

As the case II linear simulations are more applicable in the regime of stellar convection, we suggest that those simulations likely provide a starting guess for how to implement Zahn (1991)’s theory in 1D stellar models. We examine this further in the next section.

## 5. A MODIFIED SOLAR MODEL

We now examine briefly how Zahn (1991)’s theory modifies a simple structure model of the Sun. We implement a simple prescription of convective penetration in MESA (Paxton et al. 2013) as follows:

1. Find the radial location of the radiative-convective boundary according to the Schwarzschild criterion,  $r_{\text{RCB}}$ . Also evaluate the value of the mixing length  $\ell$  at that location.
2. Integrate the magnitude of the convective luminosity within the convection zone,  $L_i = \int_{r_{\text{RCB}}}^{r_{\text{RCB}}+\ell} L_{\text{conv}} dr$ .
3. Following Eqn. 14 and the measured values for the horizontal dynamics in Eqn. 33, integrate  $L_o = \int_{r_{\text{RCB}}}^{r_{\text{RCB}}+\delta_p} (L_{\text{rad}} - L_{\text{rad,ad}}) dr$ , where  $L_{\text{rad}}$  is the radiative luminosity carried by  $\nabla_{\text{rad}}$  and  $L_{\text{rad,ad}}$  is the radiative luminosity carried by  $\nabla_{\text{ad}}$ . We determine the value of  $\delta_p$  according to Eqn. 14 so that

$$C \equiv -\frac{(\bar{h}^3/\bar{h}^2)_{\text{PZ}}}{(\bar{h}^3/\bar{h}^2)_{\text{CZ}}} \approx -0.1 \Rightarrow L_o = CL_i. \quad (34)$$

4. Override the value of  $\nabla$  in the MESA solver to set  $\nabla = \nabla_{\text{ad}}$  from  $r_{\text{RCB}}$  to  $r_{\text{RCB}} - \delta_p$ .
5. Mix within this new convection zone by setting the convective velocities according to the average convective luminosity in the penetration zone,  $4\pi r^2 \rho v^3 \sim L_o$ .

We find a convection zone which extends an additional  $XH_p$  beneath the nominal Schwarzschild base of the convection zone. This results in a discontinuous temperature profile, which would result in an acoustic “glitch” on the solar frequencies. Past work has suggested from observations that the maximum depth of such an extended adiabatic region should be limited to  $0.05H_p$ , which is smaller than what is found in our model (see e.g., section 7.2.1 of Basu 2016). However, our results here are in line with the recent simulations of Käpylä (2019), which suggest an overshooting depth of  $0.2H_p$  at the base of the solar convection zone.

## 6. DISCUSSION

In this work, we discussed the theory of convective penetration put forward by Zahn (1991), then designed and analyzed two sets of simulations which showed good agreement with that theory. We furthermore examined briefly what the implications of this theory could be for a simple solar model. We find that convection zones are bounded by “penetration zones,” whose depths are determined by the shape of the radiative gradient near the convective boundaries. For the proper choice of parameters, these penetration zones can be larger than the convection zones themselves; however, for realistic stellar values ( $P_L \approx 1$ ), we find that they may be as large as 20% of the convective length scale (the mixing length in a star).

The simulations we presented in this work were the simplest possible simulations to try to test the basic tenets of Zahn (1991)’s theory. In particular, they show convincingly that the shape of the flux near the convective boundary is one of the factors that determines the depth of the penetration zone. However, as discussed in Eqns. 14 & 34, the structure of the penetrative convective flows is the other crucial ingredient in Zahn’s theory. The scalar numerical estimates for how these dynamic should be handled in the theory, presented in Eqn. 33, of course come with the caveat that the local, Cartesian, Boussinesq flows studied here may be quite different from stars where spherical effects and density stratification come into account. Future work should aim to determine how much the values in Eqn. 33 vary when these more realistic effects are taken into account.

Furthermore, it is important to note that stellar opacities, and thus stellar conductivities, are functions of thermodynamic variables rather than radial location. As a result, the formation of a penetration zone will in turn affect the conductivity profile and  $\nabla_{\text{rad}}$ , which will in turn affect the estimate of how deep a penetration zone should form. Future studies should follow e.g., Käpylä et al. (2017); Käpylä (2019) and implement realistic opacity profiles which evolve self-consistently with the thermodynamic state.

One additional complication is that stellar fluid dynamics exist in the regime of  $\text{Pr} \ll 1$  (Garaud 2021). Dynamics in this regime may be different from those in the regime of  $\text{Pr} \lesssim 1$  that we studied here, which could affect flow morphologies and thus penetration depths. Recently, Käpylä (2021) found that convective flows exhibited more overshoot at low  $\text{Pr}$  than high  $\text{Pr}$ . Future work should aim to understand how strongly the (TODO: symbol for h integrals) fraction depends on  $\text{Pr}$ .

Finally, we note that our work here assumes a uniform composition through the convective and radiative region. Frequently within stars, convective boundaries coincide with discontinuities in composition profiles (Salaris & Cassisi 2017). Future work should also aim to determine if stabilizing composition gradients can prevent the formation of penetration zones seen here (as in Fig. 1).

In summary, we have provided a first step towards deconstructing the mysteries of the behavior of convection near convective boundaries. We find that the simple-but-elegant theory of Zahn (1991) provides an excellent starting point for building a better understanding of the nature of convective penetration in stellar interiors. In future work, we will aim to more robustly implement Zahn’s theory into MESA.

<sup>1</sup> We’d like to thank Keaton Burns and Kyle Augustson for useful discussions which improved the content of this  
<sup>2</sup> manuscript. EHA is funded as a CIERA Postdoctoral fellow and would like to thank CIERA and Northwestern  
<sup>3</sup> University. Computations were conducted with support from the NASA High End Computing (HEC) Program through  
<sup>4</sup> the NASA Advanced Supercomputing (NAS) Division at Ames Research Center on Pleiades with allocation GID s2276.

### A. ACCELERATED EVOLUTION

As demonstrated in Fig. 1, the time evolution of simulations which start from a state based on the Schwarzschild criterion can be prohibitively long. In Anders et al. (2018), we explored the long time evolution of simple convective simulations and found that fast-forwarding the evolution of a convective simulation's internal energy and thermal structure is possible. In this work, we accelerate the evolution of our simulations in order to more quickly determine the final size of the evolved penetration zones according to the following algorithm.

1. Once a simulation has a volume-averaged Reynolds number greater than 1, we wait 50 freefall times.
2. We measure the 50% departure point ( $\delta_p$ ) of the top of the convection zone every freefall time, and store this information for 50 freefall times.
3. We measure  $d\delta_p/dt$  using NumPy's `gradient` function. If the average value of  $d\delta_p/dt$  has a different sign over the first and last 25 freefall times in our collection window, we erase the first 25 freefall times of data and return to step 2 for 25 freefall times. If the average value of  $d\delta_p/dt$  has the same sign over the first and last 25 freefall times, we accelerate the evolution of our simulations.
4. We calculate  $\Delta\delta_p$  as the minimum of

$$\Delta\delta_{p,1} = \frac{\overline{d\delta_p}}{dt} \left| \frac{\Delta\delta_p}{\Delta d\delta_p/dt} \right|, \quad \Delta\delta_{p,2} = 500 \frac{\overline{d\delta_p}}{dt}. \quad (\text{A1})$$

Here,  $\Delta\delta_{p,1}$  essentially represents a newton iteration in  $d\delta_p/dt$  vs.  $\delta_p$  space towards the root value where  $d\delta_p/dt = 0$ . In some cases,  $\Delta\delta_{p,1}$  becomes too large; we thus limit the maximum change to  $\Delta\delta_{p,2}$ , which represents an advancement of the convective boundary at the current evolutionary pace by 500 freefall time units.

5. After determining a new value of  $\delta_{p,\text{ev}} = \delta_{p,0} + \Delta\delta_p$ , we adjust the  $m = 0$  temperature gradient to

$$\partial_z \bar{T} = -\nabla_{\text{ad}} - H(z; \delta_{p,\text{ev}}, 0.05) \Delta \nabla, \quad (\text{A2})$$

where  $H$  is defined in Eqn. 30 and  $\Delta \nabla = \nabla_{\text{rad}} - \nabla_{\text{ad}}$ . We also multiply the temperature perturbations and full convective velocity field by  $H(z; 1, 0.05)$ . This sets all fluctuations above the nominal Schwarzschild convection zone to zero, thereby avoiding any strange dynamical transients caused by the the old dynamics at the radiative-convective boundary (which has moved as a result of this process).

6. We restart from step 1.

If a simulation returns to step 2 from step 3 ten times over the course of its evolution, we assume that it has converged near its answer, stop this iterative loop, and allow the simulation to timestep normally. This process effectively removes the long diffusive thermal evolution on display in the middle panel of Fig. 1 by immediately setting the mean temperature profile to the radiative profile above the PZ.

In Fig. 5, we display the time evolution of the same simulation as in Fig. 1, and we compare it to three simulations which use this accelerated evolution procedure. We start these three simulations with initial temperature profiles defined by Eqn. A2 with initial values of  $\delta_{p,\text{ev}} = 0$  (red line),  $\delta_{p,\text{ev}} = 0.4$  (purple line), or  $\delta_{p,\text{ev}} = 0.7$  (green line). For these simulations, we expect the evolved penetration zone depth to be  $\delta_p \approx 0.55$ , so these represent perturbations above and below this estimate, as well as the classical Schwarzschild initial conditions. While the simulation that we straightforwardly timestep (black line) takes tens of thousands of time units to reach the final state, the accelerated simulations reach the final state over the course of hundreds of freefall times.

### B. TABLE OF SIMULATION PARAMETERS

### REFERENCES

- |  |   |
|--|---|
| Aerts, C., Christensen-Dalsgaard, J., & Kurtz, D. W. 2010, Asteroseismology (Springer) | Anders, E. H., Brown, B. P., & Oishi, J. S. 2018, Physical Review Fluids, 3, 083502, doi: <a href="https://doi.org/10.1103/PhysRevFluids.3.083502">10.1103/PhysRevFluids.3.083502</a> |
|--|---|

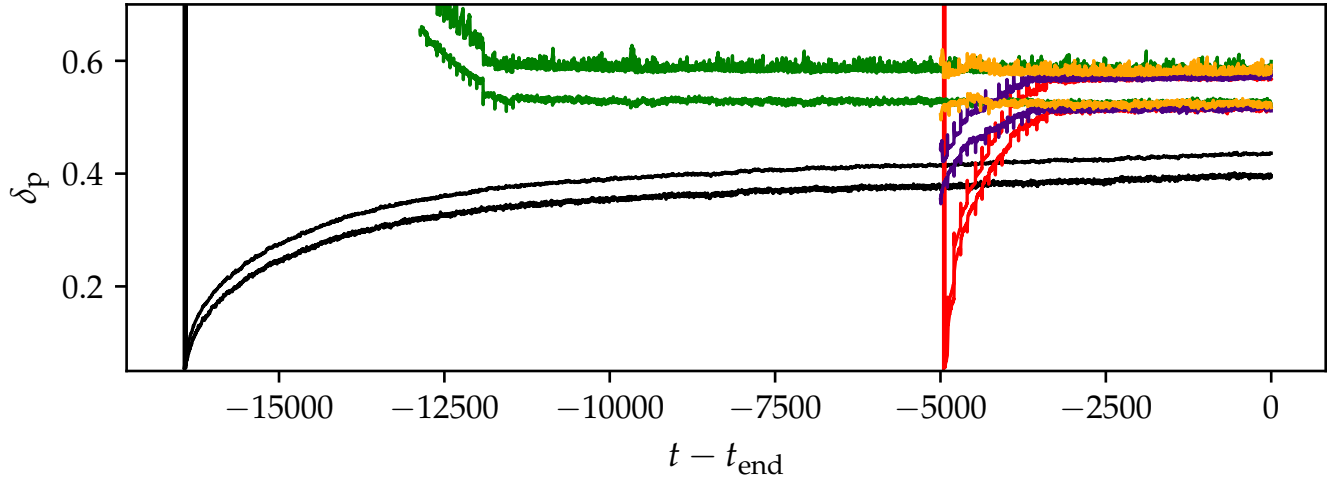


Figure 5.

- Ascher, U. M., Ruuth, S. J., & Spiteri, R. J. 1997, *Applied Numerical Mathematics*, 25, 151, doi: [https://doi.org/10.1016/S0168-9274\(97\)00056-1](https://doi.org/10.1016/S0168-9274(97)00056-1)
- Asplund, M., Amarsi, A. M., & Grevesse, N. 2021, arXiv e-prints, arXiv:2105.01661, <https://arxiv.org/abs/2105.01661>
- Bahcall, J. N., Serenelli, A. M., & Basu, S. 2005, *ApJL*, 621, L85, doi: [10.1086/428929](https://doi.org/10.1086/428929)
- Basu, S. 2016, *Living Reviews in Solar Physics*, 13, 2, doi: [10.1007/s41116-016-0003-4](https://doi.org/10.1007/s41116-016-0003-4)
- Basu, S., & Antia, H. M. 2004, *ApJL*, 606, L85, doi: [10.1086/421110](https://doi.org/10.1086/421110)
- Browning, M. K., Brun, A. S., & Toomre, J. 2004, *ApJ*, 601, 512, doi: [10.1086/380198](https://doi.org/10.1086/380198)
- Brummell, N. H., Clune, T. L., & Toomre, J. 2002, *ApJ*, 570, 825, doi: [10.1086/339626](https://doi.org/10.1086/339626)
- Brun, A. S., & Browning, M. K. 2017, *Living Reviews in Solar Physics*, 14, 4, doi: [10.1007/s41116-017-0007-8](https://doi.org/10.1007/s41116-017-0007-8)
- Brun, A. S., Strugarek, A., Varela, J., et al. 2017, *ApJ*, 836, 192, doi: [10.3847/1538-4357/aa5c40](https://doi.org/10.3847/1538-4357/aa5c40)
- Burns, K. J., Vasil, G. M., Oishi, J. S., Lecoanet, D., & Brown, B. P. 2020, *Physical Review Research*, 2, 023068, doi: [10.1103/PhysRevResearch.2.023068](https://doi.org/10.1103/PhysRevResearch.2.023068)
- Carlos, M., Meléndez, J., Spina, L., et al. 2019, *MNRAS*, 485, 4052, doi: [10.1093/mnras/stz681](https://doi.org/10.1093/mnras/stz681)
- Caswell, T. A., Droettboom, M., Lee, A., et al. 2021, *matplotlib/matplotlib: REL: v3.3.4*, Zenodo, doi: [10.5281/zenodo.4475376](https://doi.org/10.5281/zenodo.4475376)
- Christensen-Dalsgaard, J. 2021, *Living Reviews in Solar Physics*, 18, 2, doi: [10.1007/s41116-020-00028-3](https://doi.org/10.1007/s41116-020-00028-3)
- Christensen-Dalsgaard, J., Monteiro, M. J. P. F. G., Rempel, M., & Thompson, M. J. 2011, *MNRAS*, 414, 1158, doi: [10.1111/j.1365-2966.2011.18460.x](https://doi.org/10.1111/j.1365-2966.2011.18460.x)
- Claret, A., & Torres, G. 2018, *ApJ*, 859, 100, doi: [10.3847/1538-4357/aabd35](https://doi.org/10.3847/1538-4357/aabd35)
- Couston, L. A., Lecoanet, D., Favier, B., & Le Bars, M. 2017, *Physical Review Fluids*, 2, 094804, doi: [10.1103/PhysRevFluids.2.094804](https://doi.org/10.1103/PhysRevFluids.2.094804)
- Currie, L. K., & Browning, M. K. 2017, *ApJL*, 845, L17, doi: [10.3847/2041-8213/aa8301](https://doi.org/10.3847/2041-8213/aa8301)
- Deardorff, J. W., Willis, G. E., & Lilly, D. K. 1969, *Journal of Fluid Mechanics*, 35, 7, doi: [10.1017/S0022112069000942](https://doi.org/10.1017/S0022112069000942)
- Dietrich, W., & Wicht, J. 2018, *Frontiers in Earth Science*, 6, 189, doi: [10.3389/feart.2018.00189](https://doi.org/10.3389/feart.2018.00189)
- Dumont, T., Palacios, A., Charbonnel, C., et al. 2021, *A&A*, 646, A48, doi: [10.1051/0004-6361/202039515](https://doi.org/10.1051/0004-6361/202039515)
- Farmer, R., Renzo, M., de Mink, S. E., Marchant, P., & Justham, S. 2019, *ApJ*, 887, 53, doi: [10.3847/1538-4357/ab518b](https://doi.org/10.3847/1538-4357/ab518b)
- Garaud, P. 2021, *Physical Review Fluids*, 6, 030501, doi: [10.1103/PhysRevFluids.6.030501](https://doi.org/10.1103/PhysRevFluids.6.030501)
- Goluskin, D., & van der Poel, E. P. 2016, *Journal of Fluid Mechanics*, 791, R6, doi: [10.1017/jfm.2016.69](https://doi.org/10.1017/jfm.2016.69)
- Hansen, C. J., Kawaler, S. D., & Trimble, V. 2004, *Stellar interiors : physical principles, structure, and evolution* (Springer)
- Herwig, F. 2000, *A&A*, 360, 952, <https://arxiv.org/abs/astro-ph/0007139>
- Higgins, E. R., & Vink, J. S. 2020, *A&A*, 635, A175, doi: [10.1051/0004-6361/201937374](https://doi.org/10.1051/0004-6361/201937374)
- Higl, J., Müller, E., & Weiss, A. 2021, *A&A*, 646, A133, doi: [10.1051/0004-6361/202039532](https://doi.org/10.1051/0004-6361/202039532)
- Hotta, H. 2017, *ApJ*, 843, 52, doi: [10.3847/1538-4357/aa784b](https://doi.org/10.3847/1538-4357/aa784b)



- Hunter, J. D. 2007, *Computing in Science and Engineering*, 9, 90, doi: [10.1109/MCSE.2007.55](https://doi.org/10.1109/MCSE.2007.55)
- Hurlburt, N. E., Toomre, J., & Massaguer, J. M. 1986, *ApJ*, 311, 563, doi: [10.1086/164796](https://doi.org/10.1086/164796)
- Hurlburt, N. E., Toomre, J., Massaguer, J. M., & Zahn, J.-P. 1994, *ApJ*, 421, 245, doi: [10.1086/173642](https://doi.org/10.1086/173642)
- Jermyn, A. S., Tout, C. A., & Chitre, S. M. 2018, *MNRAS*, 480, 5427, doi: [10.1093/mnras/sty1831](https://doi.org/10.1093/mnras/sty1831)
- Jørgensen, A. C. S., & Weiss, A. 2019, *MNRAS*, 488, 3463, doi: [10.1093/mnras/stz1980](https://doi.org/10.1093/mnras/stz1980)
- Käpylä, P. J. 2019, *A&A*, 631, A122, doi: [10.1051/0004-6361/201834921](https://doi.org/10.1051/0004-6361/201834921)
- . 2021, arXiv e-prints, arXiv:2105.08453. <https://arxiv.org/abs/2105.08453>
- Käpylä, P. J., Korpi, M. J., Stix, M., & Tuominen, I. 2007, in *Convection in Astrophysics*, ed. F. Kupka, I. Roxburgh, & K. L. Chan, Vol. 239, 437–442, doi: [10.1017/S1743921307000865](https://doi.org/10.1017/S1743921307000865)
- Käpylä, P. J., Rheinhardt, M., Brandenburg, A., et al. 2017, *ApJL*, 845, L23, doi: [10.3847/2041-8213/aa83ab](https://doi.org/10.3847/2041-8213/aa83ab)
- Kitiashvili, I. N., Kosovichev, A. G., Mansour, N. N., & Wray, A. A. 2016, *ApJL*, 821, L17, doi: [10.3847/2041-8205/821/1/L17](https://doi.org/10.3847/2041-8205/821/1/L17)
- Korre, L., Garaud, P., & Brummell, N. H. 2019, *MNRAS*, 484, 1220, doi: [10.1093/mnras/stz047](https://doi.org/10.1093/mnras/stz047)
- Maeder, A. 1975, *A&A*, 40, 303
- Marcus, P. S., Press, W. H., & Teukolsky, S. A. 1983, *ApJ*, 267, 795, doi: [10.1086/160915](https://doi.org/10.1086/160915)
- Martinet, S., Meynet, G., Ekström, S., et al. 2021, *A&A*, 648, A126, doi: [10.1051/0004-6361/202039426](https://doi.org/10.1051/0004-6361/202039426)
- Moore, D. R., & Weiss, N. O. 1973, *Journal of Fluid Mechanics*, 61, 553, doi: [10.1017/S0022112073000868](https://doi.org/10.1017/S0022112073000868)
- Musman, S. 1968, *Journal of Fluid Mechanics*, 31, 343, doi: [10.1017/S0022112068000194](https://doi.org/10.1017/S0022112068000194)
- Paxton, B., Bildsten, L., Dotter, A., et al. 2011, *ApJS*, 192, 3, doi: [10.1088/0067-0049/192/1/3](https://doi.org/10.1088/0067-0049/192/1/3)
- Paxton, B., Cantiello, M., Arras, P., et al. 2013, *ApJS*, 208, 4, doi: [10.1088/0067-0049/208/1/4](https://doi.org/10.1088/0067-0049/208/1/4)
- Paxton, B., Schwab, J., Bauer, E. B., et al. 2018, *ApJS*, 234, 34, doi: [10.3847/1538-4365/aaa5a8](https://doi.org/10.3847/1538-4365/aaa5a8)
- Paxton, B., Smolec, R., Schwab, J., et al. 2019, *ApJS*, 243, 10, doi: [10.3847/1538-4365/ab2241](https://doi.org/10.3847/1538-4365/ab2241)
- Pedersen, M. G., Aerts, C., Pápics, P. I., et al. 2021, arXiv e-prints, arXiv:2105.04533. <https://arxiv.org/abs/2105.04533>
- Pinsonneault, M. 1997, *ARA&A*, 35, 557, doi: [10.1146/annurev.astro.35.1.557](https://doi.org/10.1146/annurev.astro.35.1.557)
- Pratt, J., Baraffe, I., Goffrey, T., et al. 2017, *A&A*, 604, A125, doi: [10.1051/0004-6361/201630362](https://doi.org/10.1051/0004-6361/201630362)
- Rempel, M. 2004, *ApJ*, 607, 1046, doi: [10.1086/383605](https://doi.org/10.1086/383605)
- Rogers, T. M., & Glatzmaier, G. A. 2005, *ApJ*, 620, 432, doi: [10.1086/423415](https://doi.org/10.1086/423415)
- Rogers, T. M., Glatzmaier, G. A., & Jones, C. A. 2006, *ApJ*, 653, 765, doi: [10.1086/508482](https://doi.org/10.1086/508482)
- Saikia, E., Singh, H. P., Chan, K. L., Roxburgh, I. W., & Srivastava, M. P. 2000, *ApJ*, 529, 402, doi: [10.1086/308249](https://doi.org/10.1086/308249)
- Salaris, M., & Cassisi, S. 2017, *Royal Society Open Science*, 4, 170192, doi: [10.1098/rsos.170192](https://doi.org/10.1098/rsos.170192)
- Shaviv, G., & Salpeter, E. E. 1973, *ApJ*, 184, 191, doi: [10.1086/152318](https://doi.org/10.1086/152318)
- Singh, H. P., Roxburgh, I. W., & Chan, K. L. 1995, *A&A*, 295, 703
- . 1998, *A&A*, 340, 178
- Spiegel, E. A., & Veronis, G. 1960, *ApJ*, 131, 442, doi: [10.1086/146849](https://doi.org/10.1086/146849)
- Tian, C.-L., Deng, L.-C., & Chan, K.-L. 2009, *MNRAS*, 398, 1011, doi: [10.1111/j.1365-2966.2009.15178.x](https://doi.org/10.1111/j.1365-2966.2009.15178.x)
- Toppaladoddi, S., & Wettlaufer, J. S. 2018, *Physical Review Fluids*, 3, 043501, doi: [10.1103/PhysRevFluids.3.043501](https://doi.org/10.1103/PhysRevFluids.3.043501)
- Viallet, M., Meakin, C., Prat, V., & Arnett, D. 2015, *A&A*, 580, A61, doi: [10.1051/0004-6361/201526294](https://doi.org/10.1051/0004-6361/201526294)
- Viani, L. S., & Basu, S. 2020, *ApJ*, 904, 22, doi: [10.3847/1538-4357/abba17](https://doi.org/10.3847/1538-4357/abba17)
- Vinyoles, N., Serenelli, A. M., Villante, F. L., et al. 2017, *ApJ*, 835, 202, doi: [10.3847/1538-4357/835/2/202](https://doi.org/10.3847/1538-4357/835/2/202)
- Woosley, S. E., Heger, A., & Weaver, T. A. 2002, *Reviews of Modern Physics*, 74, 1015, doi: [10.1103/RevModPhys.74.1015](https://doi.org/10.1103/RevModPhys.74.1015)
- Zahn, J. P. 1991, *A&A*, 252, 179